ADVANCED OPTICAL MATERIALS
www.advopticalmat.de

Smectic Defect Engineering Enabled by Programmable Photoalignment

Sai-Bo Wu, Ling-Ling Ma, Peng Chen, Hui-Min Cao, Shi-Jun Ge, Rui Yuan, Wei Hu, and Yan-Qing Lu**

Topological defects are vital for tailoring soft matter properties and inspiring remarkable applications. Arbitrary guiding and dynamic tuning of director distributions are highly pursued in defect engineering of liquid crystals. Till now, the orientation control of smectic defect walls remains a challenge. Here, photoalignment is adopted to preset the surface anchoring in order to guide smectic oily streaks. Flexible defect engineering such as deflecting, bending, and splaying is demonstrated. Based on their combination, more complicated defect arrays are realized in a predictable manner. After electric stimuli involved, new functions of tunability and rotatability are unlocked. This work brings new insights to soft matter architectures, and will upgrade the existing micromachines, nanoparticle manipulations and advanced photonic applications.

Defects, commonly originated from structural discontinuity or symmetry breaking, have aroused considerable attention in material science and inspired enormous applications, including catalysis, sensing, energy storage, and optoelectronic devices.[1] Defect engineering in soft matter enables a bottom-up microfabrication strategy, which exhibits superiorities of abundant defect categories and cost-efficient manufactures. Multifarious building blocks, such as colloidal particles,[2] block copolymers[3] and surfactants,[4] have given rise to a large number of spatial defect architectures with fantastic characteristics and promising applications. Liquid crystals (LCs) are typical soft matter, whose configurations can be depicted by LC director, i.e., the statistically dominant direction of rod-like molecules. Their director fields and resultant topological defects vary distinctly in different phases.[5] According to the spatial continuity, LC defects can be divided into three representative forms: singular points in radially oriented nematics, disclination lines corresponding to the 180° turn of LC directors, as well as defect walls at the boundary between adjacent domains.[6] The anisotropic physical property and stimuli responsiveness of LCs endow this elegant state-of-matter with tunable optical and morphological behaviors.[7] Therefore, by virtue of specific LC defect engineering, optical vortex generator,[8] polarization imaging,[9] particle assembly,[10] and motion control of bacteria[11] are demonstrated. For all these applications, precise defect engineering and dynamic structure manipulation are both highly demanded.

Under antagonistic anchoring conditions, the parallel molecular layers of smectic LCs (SLCs) will periodically deform into multiple ordered defects.[12] The final configuration is an energy-minimum balance among bulk elasticity, anchoring force and surface tension. For large film thickness, SLCs tend to self-assemble into dimple-like toric focal conic domains (FCDs), possessing a pair of circle and straight line defects in orthogonal planes.[13] Upon unidirectional alignment introduced, the configurations will degrade into tilt FCDs accordingly.[14] Further reducing the layer thickness, the film becomes continuous in the direction perpendicular to the alignment, and consequently forms the oily streaks (OSs) with periodic defect walls.[15] Thanks to intrinsic lamellar structure, the order of OSs is more rigorous than those of other LC textures. Therefore, OSs have been widely explored as scaffolds to capture or orientate nanoparticles, such as semiconductor nanorods,[16] gold nanorods,[17] fluorescent nanocrystals,[18] etc. The periodic change of director orientations results in refractive index alternations, which can be used for beam steering.[19] Meanwhile, the pitch of OSs can also be effectively tuned by vertically applied electric field.[18,20] With a chiral dopant, the orientation of defect walls could be slightly rotated in a narrow temperature range.[21] Besides, concentric OS rings could be generated via thermal sublimation and further regularly addressed with geometric confinements.[22] These works are all very meaningful attempts toward dynamic control and flexible morphing of the defect walls. Nevertheless, there still exist some challenging restrictions at present. If one can arbitrarily guide and freely tune the orientation of OSs, more creative defect engineering with unprecedented characteristics and advanced applications could be expected.

S.-B. Wu, Dr. L.-L. Ma, Dr. P. Chen, H.-M. Cao, Dr. S.-J. Ge, R. Yuan, Prof. W. Hu, Prof. Y.-Q. Lu
National Laboratory of Solid State Microstructures
Key Laboratory of Intelligent Optical Sensing and Manipulation
College of Engineering and Applied Sciences
and Collaborative Innovation Center of Advanced Microstructures
Nanjing University
Nanjing 210093, China
E-mail: huwei@nju.edu.cn; yqlu@nju.edu.cn
S.-B. Wu, Dr. P. Chen, Dr. S.-J. Ge, R. Yuan, Prof. W. Hu
Institute for Smart Liquid Crystals
JITRI
Changshu 215500, China
The ORCID identification number(s) for the author(s) of this article can be found under https://doi.org/10.1002/adom.202000593.

DOI: 10.1002/adom.202000593

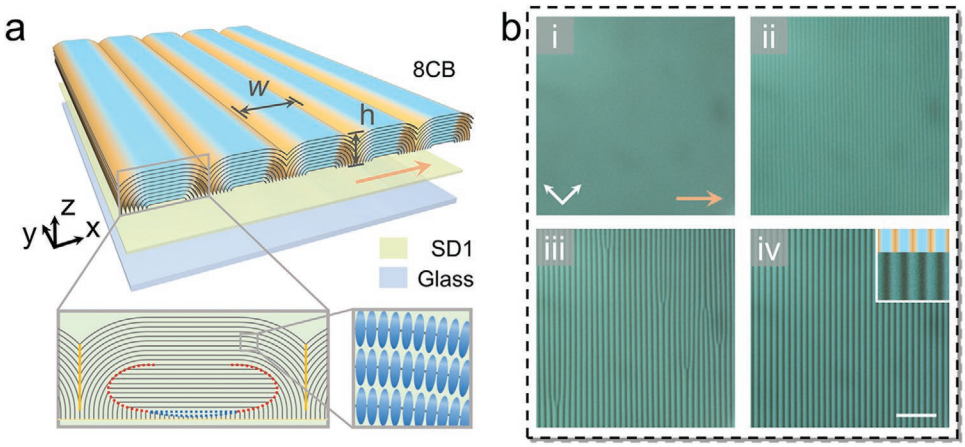

Figure 1. Defects in OSs. a) 3D illustration depicts the lamellar configuration of the OSs. Insets give the sectional layers and corresponding director distribution. b) Micrographs of the LC film during nematic-smectic phase transition under the crossed polarizers. Temperatures are b-i) 33.7 °C, b-ii) 33.5 °C, b-iii) 33.4 °C, and b-iv) 33.3 °C, respectively. Correspondence between illustration and POM image (300% amplified) is presented as an inset in (b-iv). The orange and white arrows denote the photoalignment and polarizing directions, respectively. The scale bar indicates 10 µm.

Here, a noncontact photoalignment technique is adopted to modulate the defect walls in OSs, which are always perpendicular to the surface anchoring guidance. After introducing alternative alignment domains in two different directions, zigzag defect walls are achieved. If a continuously radial alignment is preset, the defect walls would be bent to form parallel arches or spirals. In the case of an azimuthal alignment, the stripes in the OSs will change their widths slightly and generate extra branches to refill the whole space. Thereby, the defect walls could be rationally designed and arbitrarily manipulated via preprogramming the alignment conditions. When an in-plane electric field is further involved, the pitch of OSs could be tuned and the orientation of defect walls could be rotated. It enables the precise defect engineering and dynamic structure manipulation of the lamellar smectics and brings new insights to the understanding of soft matter.

In the cooling, LC changes from positionally disordered nematics to layered smectics. The parallel layers in a thin LC film will deform into a stable and regular state as illustrated in **Figure 1**a. There are several kinds of grain boundaries as marked in the sectional inset: rotating grain boundaries (red dash lines), central grain boundaries (blue dash lines) and vertical grain boundaries, i.e., defect walls (yellow solid lines).[23] The defect wall is a key feature for OS. The directors beside the wall lie along the local alignment direction and cause a phase retardation, resulting in a bright region under polarized optical microscope (POM). Meanwhile, the directors in middle areas between two neighbored defect walls are almost standing, leading to ordered dark lines. The defect wall determines the morphology of the LC film as well, which plays a vital role in various characteristics. We use photoalignment to generate a high-quality OS (Figure S1, Supporting Information). Figure 1b-i is a POM image at nematic phase, the uniform color and brightness are due to the homogeneous alignment. When temperature decreasing, defect walls appear and grow (Figure 1b-ii to iv). In the growing process, the distance between adjacent defect walls (pitch, w) increases accompanied by the generation and disappearance of forked branches.

We study the dependency of w on film thickness h (Figure S2 and Text S1, Supporting Information). As shown in **Figure 2**a, w increases linearly with h when the film thickness is below 2.25 µm. For even larger h, FCDs are obtained. For linear incident polarization parallel to the alignment direction (along x axis), the light faces a periodic refractive index change of layer-curvature-determined refractive index (n_{eff}) for defect walls and ordinary refractive index (n_o) for standing director regions between defect walls. But for the perpendicular polarization (along y axis), the light only experiences n_o. The optical anisotropy is verified by a polarization dependent diffraction. As shown in Figure 2b, two diffraction orders are distinctly observed for x polarization, while the slight widening is attributed to the nonuniformity of w. For y polarization, the diffraction totally vanishes. The polarization angle (δ) dependent diffraction efficiencies (E) of three samples with h = 0.89, 1.10, and 1.50 µm are exhibited in Figure 2c. The curves perfectly validate the optical anisotropy with high extinction ratios. As h increases, E rises up accordingly. Here the E is not high because the halfwave condition is not acquired, which could be addressed by adopting LCs with a large birefringence. As expected, the diffraction angle (α) decreases with h/w increasing (Figure 2d and Figure S3, Supporting Information).

Thanks to the guidance of photoalignment agent, the defect walls of OSs always tend to be perpendicular to the local alignments. Herein, a patterned alignment with two alternative different directions is introduced to modulate the orientations of defect walls. We systematically vary the angle between the adjacent alignments (θ_a), and study the deflecting angle (θ_d) of corresponding OSs (**Figure 3**a). In our experiments, θ_d keeps consistent with θ_a but the structures at alignment boundaries evolve with θ_a (Figure 3b–e and Figure S4, Supporting Information). When $\theta_a < 80°$, the defect walls remain continuous. In this condition, the lamellar layers tilt slightly to release the system energy (Figure 3f,g). If θ_a exceeds 80°, the configuration at the alignment boundaries degrades into FCDs (Figure 3h),[12b,24] which severely destroys the continuity of the defect walls. Upon $\theta_a > 100°$, the structures are completely divided into segments by the alignment boundaries (Figure 3i). Moreover, when θ_a is

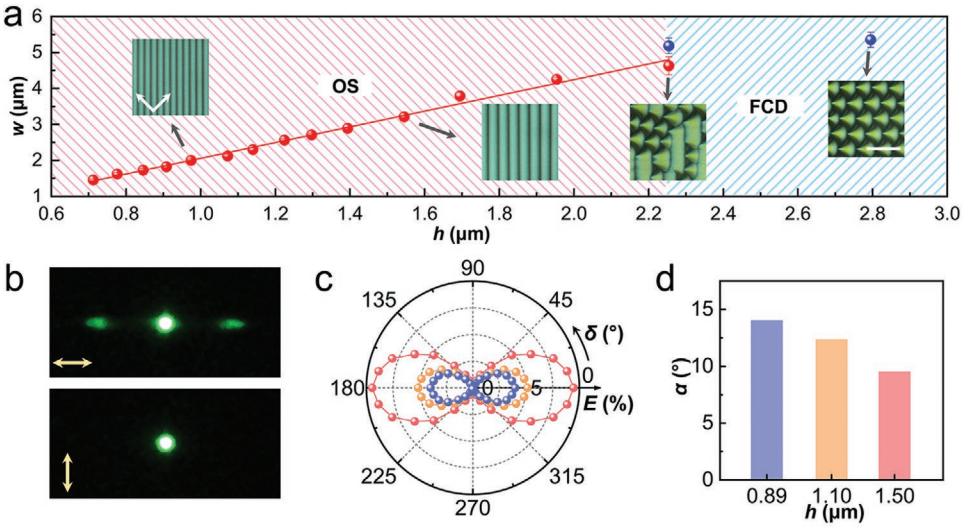

Figure 2. Structural evolution and optical characterization. a) Dependency of w on h. Insets exhibit POM images of OSs or FCDs with film thicknesses of 0.97, 1.55, 2.25, and 2.79 μm, respectively. b) Polarization-dependent diffractions. Incident polarizations are depicted by yellow arrows. c,d) Dependencies of c) E on δ, and d) α on h, respectively. The scale bar indicates 10 μm for all POM images.

close to 180°, the defect walls of neighbored alignment regions will become continuous again but with several branches (Figure S4, Supporting Information). The diffractions of these samples are characterized (Figure S5, Supporting Information). As shown in Figure 3j, four diffraction orders consistent with w are captured for the zigzag OSs, meanwhile, a series of 1D diffraction orders caused by the period (P) of the artificial photoalignment pattern are observed as well. It also reveals a polarization-dependent diffraction. Via rationally selecting θ_a, w, and P, the diffraction patterns could be freely controlled (Figure S6 and Text S2, Supporting Information).

Above facts indicate a gradient alignment variation (small θ_a condition) will induce the bending of OSs. A fan-shaped radial alignment region is carried out, whose geometry is depicted by the curvature radius (R) and central angle (θ) (**Figure 4**a). The curvature K is the reciprocal of R. For such alignment, the OSs will bend around the curvature center to form some parallel arcs (Figure 4b). As presented in Figure 4c–e, the bending of OSs and corresponding defect walls are precisely guided by the alignment in a bending curvature of zero to infinity. The azimuthal brightness variation stems from the director change, which could be more vividly revealed by color when observed under POM inserted with a tint plate.[25] When alignment direction varies from –45° to 45°, the color changes from bright yellow to dark blue. We characterize the radial and azimuthal variations of w in the sample shown in Figure 4e. w is generally constant, while the defect walls become more compact around the singularity when $K > 0.089$ μm^{-1}, i.e.,

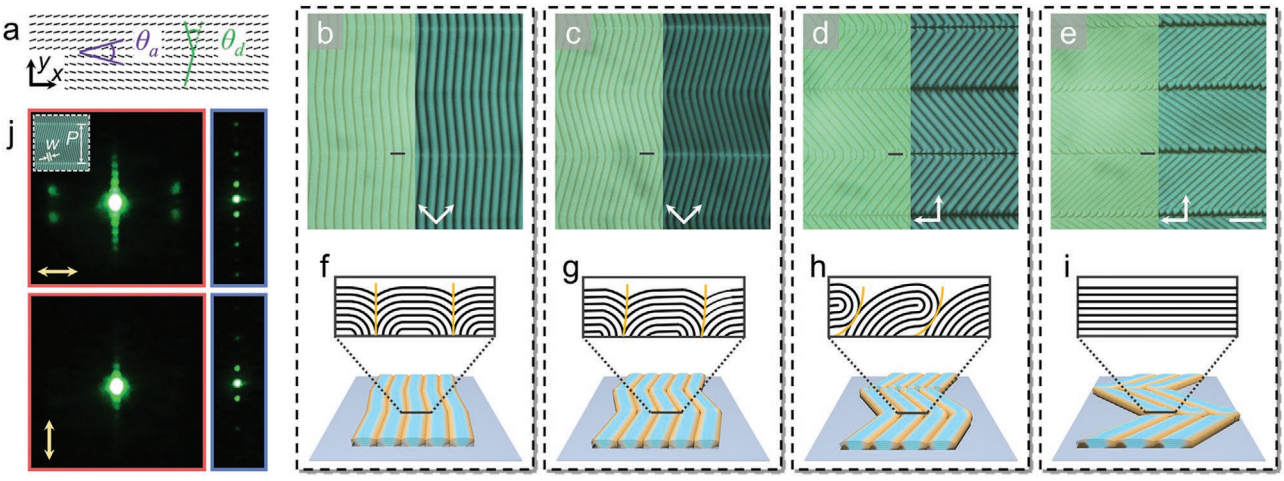

Figure 3. Zigzag defect walls. a) Scheme of photoalignment pattern. Black bars indicate local anchoring directions. b–e) Bight field (left) and POM (right) images of OSs with zigzag defect walls. θ_ds are b) 10°, c) 30°, d) 80°, and e) 100°, respectively. f–i) Corresponding 3D models of the OSs in (b–e). Insets give the sectional images at the alignment boundaries marked in (b–e). Yellow lines represent the deformed defect walls. j) Polarization-dependent diffraction patterns of (c). $w = 2.0$ μm and $P = 39.4$ μm. Distances between the sample and screens are $d_{red} = 3.5$ cm and $d_{blue} = 18.5$ cm. Incident polarizations are depicted by yellow arrows. The scale bar indicates 10 μm for all POM images.

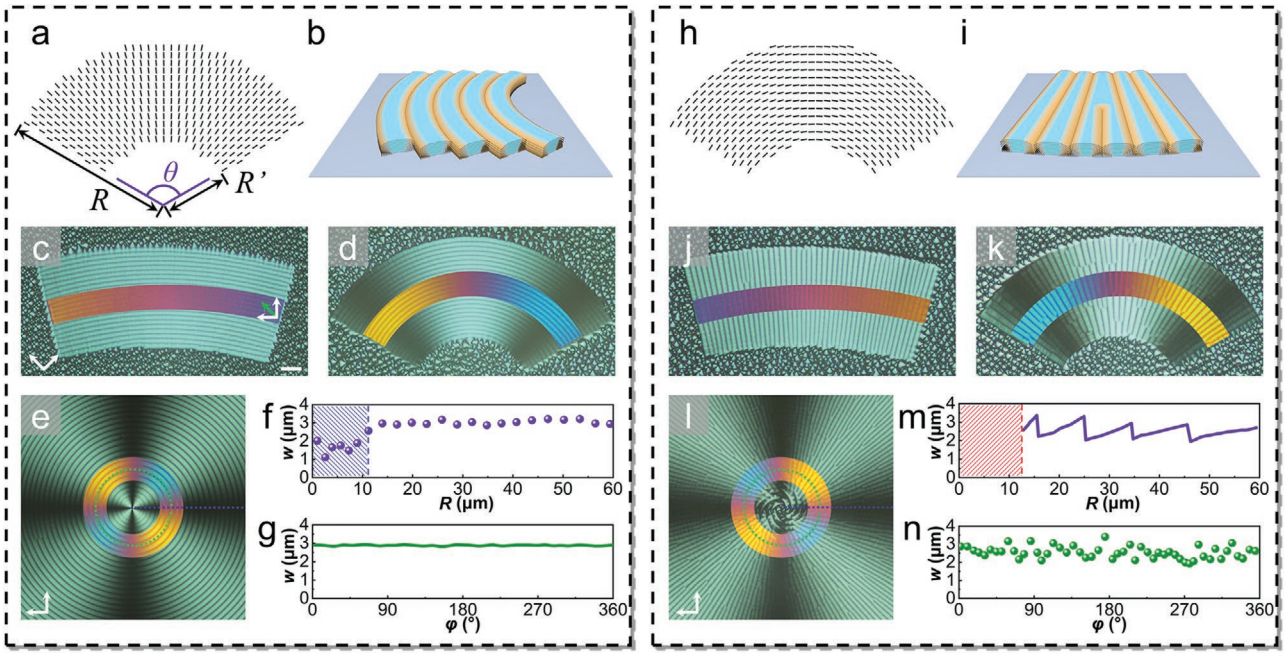

Figure 4. Bending and splaying of defect walls. a,b) Fan-shaped alignment pattern and 3D model of bent OSs. c,d) POM images of bent OSs with different R ranges and θs: c) 197.1–246.3 μm, 30° and d) 31.0–80.3 μm, 120°. e) POM image of bent OSs with K approaching infinity. f,g) Variation of w in the f) radial and g) azimuthal directions labelled by purple dashed line and green dashed circle in (e). $\varphi_{line} = 0°$ and $R_{circle} = 18.5$ μm. h,i) Fan-shaped alignment pattern and 3D model of splayed OSs. j,k) POM images of two splayed OSs. l) POM image of splayed OSs with K approaching infinity. m,n) Variation of w in the m) radial and n) azimuthal directions labelled by purple dashed line and green dashed circle in (l). The white and green arrows indicate the optical axes of the crossed polarizers and the tint plate, respectively. The scale bar indicates 10 μm for all POM images.

R < 11.2 μm (Figure 4f,g and Figure S7a,b, Supporting Information).

We rotate all initial alignments by 90° for above samples, i.e., azimuthal alignments are achieved (Figure 4h). The OSs are radially splayed with a series of branches embedded (Figure 4i). Along with the increasing of K, the defect walls split more severely, as exhibited in Figure 4j,k. When K is beyond 0.078 μm^{-1} (R < 12.8 μm), the OSs will crash and change to flower-like FCDs as exhibited in Figure 4l. This is attributed to strong boundary confinements and complex anchoring nearby the singularity. The radial and azimuthal variations of w are extracted as well (Figure 4m,n and Figure S7c,d, Supporting Information). Obviously, w is restricted to a certain range. It continuously varies in this range and abruptly decreases after the maximum accompanied with the emergence of a new branch. Additionally, the period of such variation enlarges distinctly away from the singularity.

By means of preprogramming the alignment conditions, the defect walls could be rationally designed and arbitrarily manipulated. As shown in **Figure 5**a–d, the patterns and the inner orientations of defect walls are both freely set. The different colors directly reflect corresponding alignment directions. Here the defect continuities at the alignment boundaries are more complicated, which are determined by deflected angles and array geometries of given templates. Moreover, through specifically designing the alignment condition, defect wall arrays are guided to form letters of "SLC" (Figure 5e). The in-plane orientations of defect walls are precisely guided by the local alignments (Figure 5f). These defect walls are very smooth and continuous, and the color variation indicates a gradient director change. Some merging and splitting are induced by energy fluctuation, which are unavoidable in self-assembly systems.

LCs exhibit excellent responsiveness to various external fields. That means the configuration of OSs can be tuned to reach a new equilibrium state. We set interdigitated ITO electrodes beneath the alignment layer to introduce electric stimulus (**Figure 6**a). The electric field distribution is simulated using the commercial software Techwiz LCD. As presented in Figure 6b, lateral electric fields parallel to the substrate are generated between adjacent electrodes, while vertical electric fields are formed over the electrodes. After an alignment layer is coated and unidirectionally photoaligned, straight OSs could be obtained. Moreover, the initial angle between the orientation of OSs and the electrodes (γ_0) could be freely preset (Figure 6c). In the case of $\gamma_0 = 0°$, uniformly separated defect walls are observed (Figure 6d). Due to the high viscosity of smectics, a heating and cooling across the nematic-smectic phase transition is employed to reach the new equilibrium.[26] When a voltage (20 V, 1 kHz) is applied, the w over electrodes decreases significantly (Figure 6e). As aforementioned, OSs occur at antagonistic boundary conditions, i.e., planar surface anchoring and air-induced homeotropic anchoring. Actually, the former dominates the final configuration. The vertical electric field over the electrodes can be considered as an extra contribution to the homeotropic anchoring, leading to an effect similar to reducing the film thickness. On the contrary, the lateral field over the space between adjacent electrodes contribute to planar anchoring, resulting in a slight w variation. For high

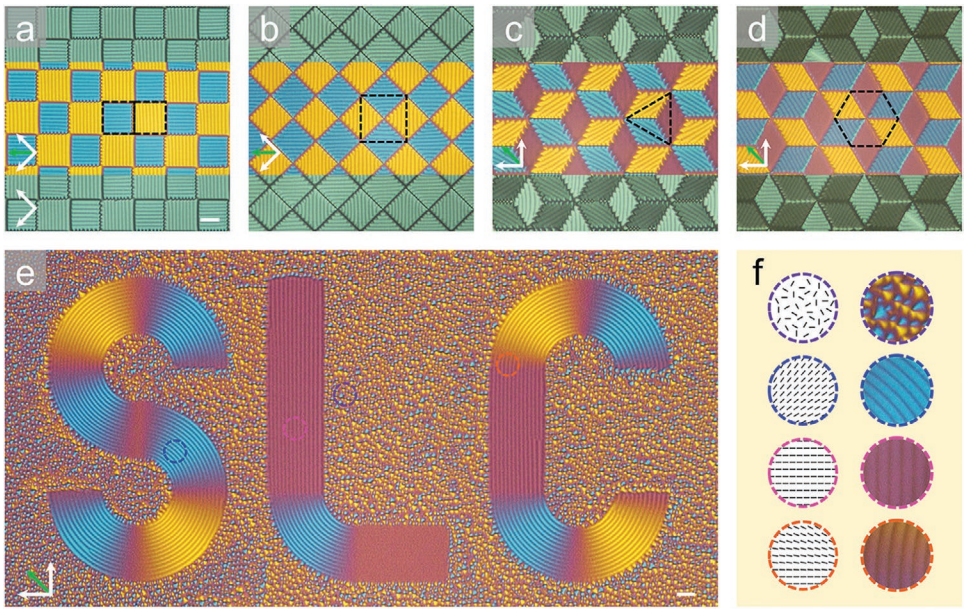

Figure 5. Patterned defect wall array. a–d) POM images of squares with orthogonal straight OSs parallel to a) sides, b) diagonals, and hexagonal rhombuses with OSs parallel to c) long diagonals, d) short diagonals. e) Letters of "SLC" formed by OSs. f) 300% amplified images of four representative regions. Black bars reveal the local alignments. All scale bars indicate 10 µm.

voltage over 80 V, LC directors will be reoriented uniaxially along the electric field between electrodes, whereas regions over electrodes remain OSs (Figure 6f). We further set $\gamma_0 = 45°$ (Figure 6g). As 20 V applied, the defect walls between the electrodes rotate anticlockwise by 19° (Figure 6h) to balance the different w variations of the neighbored areas to form continuous OSs, which is benefit for minimizing the system energy. A uniaxial orientation is also achieved over 90 V (Figure 6i).

In this work, by preprogramming the alignment condition, the deflecting, bending and splaying manipulations of smectic defect walls are presented. Based on the flexible combination of above three elemental forms, more complicated defect engineering could be realized in a predictable manner. As a self-assembly strategy, the proposed method shows the merits of simplicity, high efficiency and good feasibility for large-scale production. Via introducing specific electric field distribution, both width and orientation of OSs are manipulated, and even their switch on/off are demonstrated. This brings the dynamic control to the state-of-the-art systems. Actually, other external stimuli, such as light, heat, force and sound, can be utilized to trigger the structure transformation as well. This ordered soft matter provides a powerful platform for micromachines, nanoparticle manipulations, and beam steering with intrinsic polarization-selectivity. The correspondence of diffraction characteristics on configurations, combined with the responsiveness of LCs to external stimuli, would enable the sensing for versatile physical properties.

In all, we present a strategy for arbitrary guiding and flexible tuning of smectic defect walls by virtue of predesigned alignment conditions and electric field stimuli. Through

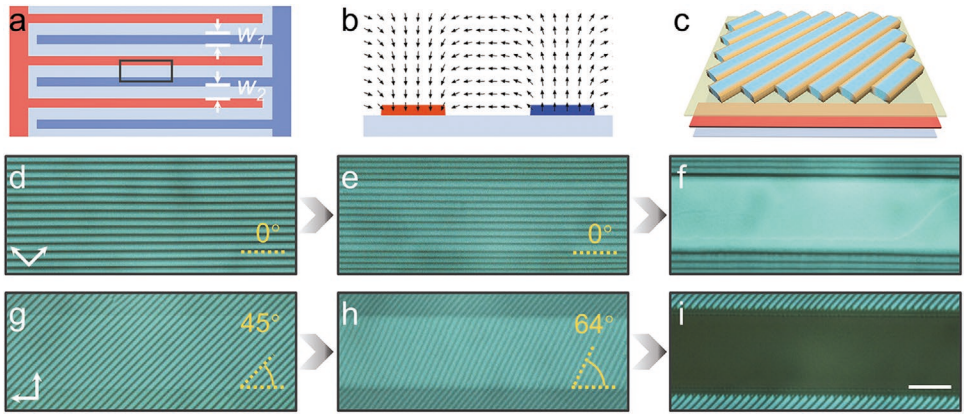

Figure 6. Dynamic electrical control of defect walls. a) Schematic diagram of the interdigitated ITO electrodes: w_1 = 12.0 µm and w_2 = 15.5 µm. b) Simulated sectional electric field distribution. c) 3D model of straight OSs on the IPS substrate. d–f) POM images of OSs ($\gamma_0 = 0°$) driven by electric fields of d) 0 V, e) 20 V, and f) 80 V, respectively. g–i) POM images of OSs ($\gamma_0 = 45°$) driven by electric fields of g) 0 V, h) 20 V, and i) 90 V, respectively. The scale bar indicates 10 µm for all POM images.

rationally combining the deflecting, bending and splaying of OSs, free defect engineering is verified. The assistance of electric field further unlocks the tunability and rotatability of the regular defect arrays. This work will extend the understanding of soft matter architectures, release more creative defect engineering with unprecedented characteristics, upgrade existing micromachining techniques and inspire advanced photonic applications.

Experimental Section

Materials: The SLC material 8CB (HCCH, China) has a nematic–smectic transition at 33.5 °C. The photoalignment agent sulfonic azo dye SD1 (Dai-Nippon Ink and Chemicals, Japan) was dissolved in dimethylformamide (DMF) at a concentration of 0.3 wt%.

Sample Fabrication: Glass substrates were ultrasonically washed, UV–ozone cleaned and spin-coated with SD1 successively. After curing at 100 °C for 10 min, SD1 layers were photopatterned via a dynamic polarization microlithography system.[27] Subsequently, 8CB was cast onto the alignment layers and heated to 80 °C, followed by a spin-coating process for 30 s. The formed LC films were held at 38 °C (nematic phase) for 2 min to eliminate dislocations, and then cooled to 33 °C (smectic phase) at a rate of 0.2 °C min^{-1} to generate OSs.

Optical Characterization: Texture observations were performed on a polarized optical microscope (Nikon 50i, Japan) with or without a retardation plate (530 nm). For the diffraction measurements, a linearly polarized supercontinuum fiber laser (SuperK EVO, NKT Photonics, Denmark) filtered at $\lambda = 532$ nm was normally incident onto the sample (Figure S5, Supporting Information). Diffraction patterns were captured by a digital camera (EOS M Canon, Japan) on different screens.

Supporting Information

Supporting Information is available from the Wiley Online Library or from the author.

Acknowledgements

The authors gratefully acknowledge the support of the National Natural Science Foundation of China (NSFC) (61922038), the National Key Research and Development Program of China (2017YFA0303700), the Fundamental Research Funds for the Central Universities (14380170), the Distinguished Young Scholars Fund of Jiangsu Province (BK20180004) and the Tang Scholar program.

Conflict of Interest

The authors declare no conflict of interest.

Keywords

defect engineering, electric stimuli, liquid crystals, photoalignment, self-assembly

Received: April 7, 2020
Revised: May 19, 2020
Published online: June 8, 2020

[1] a) C. Tang, H. F. Wang, X. Chen, B. Q. Li, T. Z. Hou, B. Zhang, Q. Zhang, M. M. Titirici, F. Wei, *Adv. Mater.* **2016**, *28*, 6845; b) O. V. Yazyev, S. G. Louie, *Phys. Rev. B* **2010**, *81*, 195420; c) D.-Y. Son, S.-G. Kim, J.-Y. Seo, S.-H. Lee, H. Shin, D. Lee, N.-G. Park, *J. Am. Chem. Soc.* **2018**, *140*, 1358; d) P. K. Chow, R. B. Jacobs-Gedrim, J. Gao, T.-M. Lu, B. Yu, H. Terrones, N. Koratkar, *ACS Nano* **2015**, *9*, 1520.

[2] a) F. Li, D. P. Josephson, A. Stein, *Angew. Chem., Int. Ed.* **2011**, *50*, 360; b) J. Zhang, Z. Zhu, Z. Yu, L. Ling, C.-F. Wang, S. Chen, *Mater. Horiz.* **2019**, *6*, 90.

[3] C. M. Bates, M. J. Maher, D. W. Janes, C. J. Ellison, C. G. Willson, *Macromolecules* **2014**, *47*, 2.

[4] M. R. Song, J. Ju, S. Q. Luo, Y. C. Han, Z. C. Dong, Y. L. Wang, Z. Gu, L. J. Zhang, R. R. Hao, L. Jiang, *Sci. Adv.* **2017**, *3*, 7.

[5] a) M. Kleman, O. D. Lavrentovich, *Liq. Cryst.* **2009**, *36*, 1085; b) J.-I. Fukuda, S. Žumer, *Phys. Rev. Lett.* **2010**, *104*, 017801; c) J.-S. B. Tai, I. I. Smalyukh, *Science* **2019**, *365*, 1449; d) H. Yoshida, K. Asakura, J. Fukuda, M. Ozaki, *Nat. Commun.* **2015**, *6*, 7180.

[6] P.-G. De Gennes, J. Prost, *The Physics of Liquid Crystals*, Oxford University Press, Oxford, UK **1993**.

[7] R. Chen, Y. H. Lee, T. Zhan, K. Yin, Z. An, S. T. Wu, *Adv. Opt. Mater.* **2019**, *7*, 1900101.

[8] P. Salamon, N. Eber, Y. Sasaki, H. Orihara, A. Buka, F. Araoka, *Phys. Rev. Appl.* **2018**, *10*, 13.

[9] L.-L. Ma, S.-B. Wu, W. Hu, C. Liu, P. Chen, H. Qian, Y. Wang, L. Chi, Y.-Q. Lu, *ACS Nano* **2019**, *13*, 13709.

[10] a) H. Mundoor, G. H. Sheetah, S. Park, P. J. Ackerman, I. I. Smalyukh, J. van de Lagemaat, *ACS Nano* **2018**, *12*, 2580; b) X. Wang, D. S. Miller, E. Bukusoglu, J. J. de Pablo, N. L. Abbott, *Nat. Mater.* **2016**, *15*, 106.

[11] C. Peng, T. Turiv, Y. Guo, Q.-H. Wei, O. D. Lavrentovich, *Science* **2016**, *354*, 882.

[12] a) J. B. Fournier, I. Dozov, G. Durand, *Phys. Rev. A* **1990**, *41*, 2252; b) L. L. Ma, M. J. Tang, W. Hu, Z. Q. Cui, S. J. Ge, P. Chen, L. J. Chen, H. Qian, L. F. Chi, Y. Q. Lu, *Adv. Mater.* **2017**, *29*, 1606671; c) Y. H. Kim, D. K. Yoon, M. C. Choi, H. S. Jeong, M. W. Kim, O. D. Lavrentovich, H. T. Jung, *Langmuir* **2009**, *25*, 1685; d) Y. Xia, A. Honglawan, S. Yang, *Liq. Cryst. Rev.* **2019**, *7*, 30.

[13] D. K. Yoon, M. C. Choi, Y. H. Kim, M. W. Kim, O. D. Lavrentovich, H. T. Jung, *Nat. Mater.* **2007**, *6*, 866.

[14] B. Zappone, C. Meyer, L. Bruno, E. Lacaze, *Soft Matter* **2012**, *8*, 4318.

[15] a) J. P. Michel, E. Lacaze, M. Goldmann, M. Gailhanou, M. De Boissieu, M. Alba, *Phys. Rev. Lett.* **2006**, *96*, 027803; b) J. P. Michel, E. Lacaze, M. Alba, M. De Boissieu, M. Gailhanou, M. Goldmann, *Phys. Rev. E* **2004**, *70*, 011709.

[16] L. Pelliser, M. Manceau, C. Lethiec, D. Coursault, S. Vezzoli, G. Leménager, L. Coolen, M. DeVittorio, F. Pisanello, L. Carbone, A. Maitre, A. Bramati, E. Lacaze, *Adv. Funct. Mater.* **2015**, *25*, 1719.

[17] a) B. Rozic, J. Fresnais, C. Molinaro, J. Calixte, S. Umadevi, S. Lau-Truong, N. Felidj, T. Kraus, F. Charra, V. Dupuis, T. Hegmann, C. Fiorini-Debuisschert, B. Gallas, E. Lacaze, *ACS Nano* **2017**, *11*, 6728; b) S.-P. Do, A. Missaoui, A. Coati, D. Coursault, H. Jeridi, A. Resta, N. Goubet, M. M. Wojcik, A. Choux, S. Royer, E. Briand, B. Donnio, J. L. Gallani, B. Pansu, E. Lhuillier, Y. Garreau, D. Babonneau, M. Goldmann, D. Constantin, B. Gallas, B. Croset, E. Lacaze, *Nano Lett.* **2020**, *20*, 1598.

[18] I. Gryn, E. Lacaze, L. Carbone, M. Giocondo, B. Zappone, *Adv. Funct. Mater.* **2016**, *26*, 7122.

[19] R. S. Zola, H. K. Bisoyi, H. Wang, A. M. Urbas, T. J. Bunning, Q. Li, *Adv. Mater.* **2019**, *31*, 1806172.

[20] I. Gryn, E. Lacaze, R. Bartolino, B. Zappone, *Adv. Funct. Mater.* **2015**, *25*, 142.

[21] I. R. Nemitz, A. J. Ferris, E. Lacaze, C. Rosenblatt, *Soft Matter* **2016**, *12*, 6662.
[22] a) D. K. Yoon, Y. H. Kim, D. S. Kim, S. D. Oh, I. I. Smalyukh, N. A. Clark, H. T. Jung, *Proc. Natl. Acad. Sci. USA* **2013**, *110*, 19263; b) D. S. Kim, Y. J. Cha, H. Kim, M. H. Kim, Y. H. Kim, D. K. Yoon, *RSC Adv.* **2014**, *4*, 26946.
[23] D. Coursault, B. Zappone, A. Coati, A. Boulaoued, L. Pelliser, D. Limagne, N. Boudet, B. H. Ibrahim, A. De Martino, M. Alba, M. Goldmann, Y. Garreau, B. Gallas, E. Lacaze, *Soft Matter* **2016**, *12*, 678.
[24] M. Kleman, O. D. Lavrentovich, *Eur. Phys. J. E: Soft Matter Biol. Phys.* **2000**, *2*, 47.
[25] D. S. Kim, S. Čopar, U. Tkalec, D. K. Yoon, *Sci. Adv.* **2018**, *4*, eaau8064.
[26] A. Suh, H. Ahn, T. J. Shin, D. K. Yoon, *J. Mater. Chem. C* **2019**, *7*, 1713.
[27] B. Y. Wei, W. Hu, Y. Ming, F. Xu, S. Rubin, J. G. Wang, V. Chigrinov, Y. Q. Lu, *Adv. Mater.* **2014**, *26*, 1590.